

Measurement of the top quark pair production cross section in the lepton + jets channel in proton-antiproton collisions at $\sqrt{s} = 1.96$ TeV

V. M. Abazov,³⁵ B. Abbott,⁷² B. S. Acharya,²⁹ M. Adams,⁴⁸ T. Adams,⁴⁶ G. D. Alexeev,³⁵ G. Alkhazov,³⁹ A. Alton,^{60,*} G. Alverson,⁵⁹ G. A. Alves,² L. S. Ancu,³⁴ M. Aoki,⁴⁷ M. Arov,⁵⁷ A. Askew,⁴⁶ B. Asman,⁴⁰ O. Atramentov,⁶⁴ C. Avila,⁸ J. BackusMayes,⁷⁹ F. Badaud,¹³ L. Bagby,⁴⁷ B. Baldin,⁴⁷ D. V. Bandurin,⁴⁶ S. Banerjee,²⁹ E. Barberis,⁵⁹ P. Baringer,⁵⁵ J. Barreto,³ J. F. Bartlett,⁴⁷ U. Bassler,¹⁸ V. Bazterra,⁴⁸ S. Beale,⁶ A. Bean,⁵⁵ M. Begalli,³ M. Begel,⁷⁰ C. Belanger-Champagne,⁴⁰ L. Bellantoni,⁴⁷ S. B. Beri,²⁷ G. Bernardi,¹⁷ R. Bernhard,²² I. Bertram,⁴¹ M. Besançon,¹⁸ R. Beuselinck,⁴² V. A. Bezzubov,³⁸ P. C. Bhat,⁴⁷ V. Bhatnagar,²⁷ G. Blazey,⁴⁹ S. Blessing,⁴⁶ K. Bloom,⁶³ A. Boehnlein,⁴⁷ D. Boline,⁶⁹ T. A. Bolton,⁵⁶ E. E. Boos,³⁷ G. Borissov,⁴¹ T. Bose,⁵⁸ A. Brandt,⁷⁵ O. Brandt,²³ R. Brock,⁶¹ G. Brooijmans,⁶⁷ A. Bross,⁴⁷ D. Brown,¹⁷ J. Brown,¹⁷ X. B. Bu,⁴⁷ M. Buehler,⁷⁸ V. Buescher,²⁴ V. Bunichev,³⁷ S. Burdin,^{41,†} T. H. Burnett,⁷⁹ C. P. Buszello,⁴⁰ B. Calpas,¹⁵ E. Camacho-Pérez,³² M. A. Carrasco-Lizarraga,⁵⁵ B. C. K. Casey,⁴⁷ H. Castilla-Valdez,³² S. Chakrabarti,⁶⁹ D. Chakraborty,⁴⁹ K. M. Chan,⁵³ A. Chandra,⁷⁷ G. Chen,⁵⁵ S. Chevalier-Théry,¹⁸ D. K. Cho,⁷⁴ S. W. Cho,³¹ S. Choi,³¹ B. Choudhary,²⁸ T. Christoudias,⁴² S. Cihangir,⁴⁷ D. Claes,⁶³ J. Clutter,⁵⁵ M. Cooke,⁴⁷ W. E. Cooper,⁴⁷ M. Corcoran,⁷⁷ F. Couderc,¹⁸ M.-C. Cousinou,¹⁵ A. Croc,¹⁸ D. Cutts,⁷⁴ A. Das,⁴⁴ G. Davies,⁴² K. De,⁷⁵ S. J. de Jong,³⁴ E. De La Cruz-Burelo,³² F. Déliot,¹⁸ M. Demarteau,⁴⁷ R. Demina,⁶⁸ D. Denisov,⁴⁷ S. P. Denisov,³⁸ S. Desai,⁴⁷ K. DeVaughan,⁶³ H. T. Diehl,⁴⁷ M. Diesburg,⁴⁷ A. Dominguez,⁶³ T. Dorland,⁷⁹ A. Dubey,²⁸ L. V. Dudko,³⁷ D. Duggan,⁶⁴ A. Duperrin,¹⁵ S. Dutt,²⁷ A. Dyshkant,⁴⁹ M. Eads,⁶³ D. Edmunds,⁶¹ J. Ellison,⁴⁵ V. D. Elvira,⁴⁷ Y. Enari,¹⁷ H. Evans,⁵¹ A. Evdokimov,⁷⁰ V. N. Evdokimov,³⁸ G. Facini,⁵⁹ T. Ferbel,⁶⁸ F. Fiedler,²⁴ F. Filthaut,³⁴ W. Fisher,⁶¹ H. E. Fisk,⁴⁷ M. Fortner,⁴⁹ H. Fox,⁴¹ S. Fuess,⁴⁷ T. Gadfort,⁷⁰ A. Garcia-Bellido,⁶⁸ V. Gavrilov,³⁶ P. Gay,¹³ W. Geist,¹⁹ W. Geng,^{15,61} D. Gerbaudo,⁶⁵ C. E. Gerber,⁴⁸ Y. Gershtein,⁶⁴ G. Ginther,^{47,68} G. Golovanov,³⁵ A. Goussiou,⁷⁹ P. D. Grannis,⁶⁹ S. Greder,¹⁹ H. Greenlee,⁴⁷ Z. D. Greenwood,⁵⁷ E. M. Gregores,⁴ G. Grenier,²⁰ Ph. Gris,¹³ J.-F. Grivaz,¹⁶ A. Grohsjean,¹⁸ S. Grünendahl,⁴⁷ M. W. Grünewald,³⁰ F. Guo,⁶⁹ G. Gutierrez,⁴⁷ P. Gutierrez,⁷² A. Haas,^{67,‡} S. Hagopian,⁴⁶ J. Haley,⁵⁹ L. Han,⁷ K. Harder,⁴³ A. Harel,⁶⁸ J. M. Hauptman,⁵⁴ J. Hays,⁴² T. Head,⁴³ T. Hebbeker,²¹ D. Hedin,⁴⁹ H. Hegab,⁷³ A. P. Heinson,⁴⁵ U. Heintz,⁷⁴ C. Hensel,²³ I. Heredia-De La Cruz,³² K. Herner,⁶⁰ M. D. Hildreth,⁵³ R. Hirosky,⁷⁸ T. Hoang,⁴⁶ J. D. Hobbs,⁶⁹ B. Hoeneisen,¹² M. Hohlfield,²⁴ S. Hossain,⁷² Z. Hubacek,^{10,18} N. Huske,¹⁷ V. Hynek,¹⁰ I. Iashvili,⁶⁶ R. Illingworth,⁴⁷ A. S. Ito,⁴⁷ S. Jabeen,⁷⁴ M. Jaffré,¹⁶ S. Jain,⁶⁶ D. Jamin,¹⁵ R. Jesik,⁴² K. Johns,⁴⁴ M. Johnson,⁴⁷ D. Johnston,⁶³ A. Jonckheere,⁴⁷ P. Jonsson,⁴² J. Joshi,²⁷ A. Juste,^{47,§} K. Kaadze,⁵⁶ E. Kajfasz,¹⁵ D. Karmanov,³⁷ P. A. Kasper,⁴⁷ I. Katsanos,⁶³ R. Kehoe,⁷⁶ S. Kermiche,¹⁵ N. Khalatyan,⁴⁷ A. Khanov,⁷³ A. Kharchilava,⁶⁶ Y. N. Kharzheev,³⁵ D. Khatidze,⁷⁴ M. H. Kirby,⁵⁰ J. M. Kohli,²⁷ A. V. Kozelov,³⁸ J. Kraus,⁶¹ A. Kumar,⁶⁶ A. Kupco,¹¹ T. Kurča,²⁰ V. A. Kuzmin,³⁷ J. Kvita,⁹ S. Lammers,⁵¹ G. Landsberg,⁷⁴ P. Lebrun,²⁰ H. S. Lee,³¹ S. W. Lee,⁵⁴ W. M. Lee,⁴⁷ J. Lellouch,¹⁷ L. Li,⁴⁵ Q. Z. Li,⁴⁷ S. M. Lietti,⁵ J. K. Lim,³¹ D. Lincoln,⁴⁷ J. Linnemann,⁶¹ V. V. Lipaev,³⁸ R. Lipton,⁴⁷ Y. Liu,⁷ Z. Liu,⁶ A. Lobodenko,³⁹ M. Lokajicek,¹¹ P. Love,⁴¹ H. J. Lubatti,⁷⁹ R. Luna-Garcia,^{32,||} A. L. Lyon,⁴⁷ A. K. A. Maciel,² D. Mackin,⁷⁷ R. Madar,¹⁸ R. Magaña-Villalba,³² S. Malik,⁶³ V. L. Malyshev,³⁵ Y. Maravin,⁵⁶ J. Martínez-Ortega,³² R. McCarthy,⁶⁹ C. L. McGivern,⁵⁵ M. M. Meijer,³⁴ A. Melnitchouk,⁶² D. Menezes,⁴⁹ P. G. Mercadante,⁴ M. Merkin,³⁷ A. Meyer,²¹ J. Meyer,²³ F. Miconi,¹⁹ N. K. Mondal,²⁹ G. S. Muanza,¹⁵ M. Mulhearn,⁷⁸ E. Nagy,¹⁵ M. Naimuddin,²⁸ M. Narain,⁷⁴ R. Nayyar,²⁸ H. A. Neal,⁶⁰ J. P. Negret,⁸ P. Neustroev,³⁹ S. F. Novaes,⁵ T. Nunnemann,²⁵ G. Obrant,³⁹ J. Orduna,³² N. Osman,⁴² J. Osta,⁵³ G. J. Otero y Garzón,¹ M. Owen,⁴³ M. Padilla,⁴⁵ M. Pangilinan,⁷⁴ N. Parashar,⁵² V. Parihar,⁷⁴ S. K. Park,³¹ J. Parsons,⁶⁷ R. Partridge,^{74,‡} N. Parua,⁵¹ A. Patwa,⁷⁰ B. Penning,⁴⁷ M. Perfilov,³⁷ K. Peters,⁴³ Y. Peters,⁴³ G. Petrillo,⁶⁸ P. Pétrouff,¹⁶ R. Piegaia,¹ J. Piper,⁶¹ M.-A. Pleier,⁷⁰ P. L. M. Podesta-Lerma,^{32,¶} V. M. Podstavkov,⁴⁷ M.-E. Pol,² P. Polozov,³⁶ A. V. Popov,³⁸ M. Prewitt,⁷⁷ D. Price,⁵¹ S. Protopopescu,⁷⁰ J. Qian,⁶⁰ A. Quadt,²³ B. Quinn,⁶² M. S. Rangel,² K. Ranjan,²⁸ P. N. Ratoff,⁴¹ I. Razumov,³⁸ P. Renkel,⁷⁶ M. Rijssenbeek,⁶⁹ I. Ripp-Baudot,¹⁹ F. Rizatdinova,⁷³ M. Rominsky,⁴⁷ C. Royon,¹⁸ P. Rubinov,⁴⁷ R. Ruchti,⁵³ G. Safronov,³⁶ G. Sajot,¹⁴ A. Sánchez-Hernández,³² M. P. Sanders,²⁵ B. Sanghi,⁴⁷ A. S. Santos,⁵ G. Savage,⁴⁷ L. Sawyer,⁵⁷ T. Scanlon,⁴² R. D. Schamberger,⁶⁹ Y. Scheglov,³⁹ H. Schellman,⁵⁰ T. Schliephake,²⁶ S. Schlobohm,⁷⁹ C. Schwanenberger,⁴³ R. Schwienhorst,⁶¹ J. Sekaric,⁵⁵ H. Severini,⁷² E. Shabalina,²³ V. Shary,¹⁸ A. A. Shchukin,³⁸ R. K. Shivpuri,²⁸ V. Simak,¹⁰ V. Sirotenko,⁴⁷ P. Skubic,⁷² P. Slattery,⁶⁸ D. Smirnov,⁵³ K. J. Smith,⁶⁶ G. R. Snow,⁶³ J. Snow,⁷¹ S. Snyder,⁷⁰ S. Söldner-Rembold,⁴³ L. Sonnenschein,²¹ A. Sopczak,⁴¹ M. Sosebee,⁷⁵ K. Soustruznik,⁹ B. Spurlock,⁷⁵ J. Stark,¹⁴ V. Stolin,³⁶ D. A. Stoyanova,³⁸ M. Strauss,⁷² D. Strom,⁴⁸ L. Stutte,⁴⁷ L. Suter,⁴³ P. Svoisky,⁷² M. Takahashi,⁴³ A. Tanasijczuk,¹ W. Taylor,⁶ M. Titov,¹⁸ V. V. Tokmenin,³⁵ Y.-T. Tsai,⁶⁸ D. Tsybychev,⁶⁹ B. Tuchming,¹⁸ C. Tully,⁶⁵ P. M. Tuts,⁶⁷ L. Uvarov,³⁹ S. Uvarov,³⁹ S. Uzunyan,⁴⁹ R. Van Kooten,⁵¹ W. M. van Leeuwen,³³ N. Varelas,⁴⁸

E. W. Varnes,⁴⁴ I. A. Vasilyev,³⁸ P. Verdier,²⁰ L. S. Vertogradov,³⁵ M. Verzocchi,⁴⁷ M. Vesterinen,⁴³ D. Vilanova,¹⁸ P. Vint,⁴² P. Vokac,¹⁰ H. D. Wahl,⁴⁶ M. H. L. S. Wang,⁶⁸ J. Warchol,⁵³ G. Watts,⁷⁹ M. Wayne,⁵³ M. Weber,^{47,**} L. Welty-Rieger,⁵⁰ A. White,⁷⁵ D. Wicke,²⁶ M. R. J. Williams,⁴¹ G. W. Wilson,⁵⁵ S. J. Wimpenny,⁴⁵ M. Wobisch,⁵⁷ D. R. Wood,⁵⁹ T. R. Wyatt,⁴³ Y. Xie,⁴⁷ C. Xu,⁶⁰ S. Yacoob,⁵⁰ R. Yamada,⁴⁷ W.-C. Yang,⁴³ T. Yasuda,⁴⁷ Y. A. Yatsunenko,³⁵ Z. Ye,⁴⁷ H. Yin,⁴⁷ K. Yip,⁷⁰ S. W. Youn,⁴⁷ J. Yu,⁷⁵ S. Zelitch,⁷⁸ T. Zhao,⁷⁹ B. Zhou,⁶⁰ J. Zhu,⁶⁰ M. Zielinski,⁶⁸ D. Zieminska,⁵¹ and L. Zivkovic⁷⁴

(D0 Collaboration)

¹*Universidad de Buenos Aires, Buenos Aires, Argentina*

²*LAFEX, Centro Brasileiro de Pesquisas Físicas, Rio de Janeiro, Brazil*

³*Universidade do Estado do Rio de Janeiro, Rio de Janeiro, Brazil*

⁴*Universidade Federal do ABC, Santo André, Brazil*

⁵*Instituto de Física Teórica, Universidade Estadual Paulista, São Paulo, Brazil*

⁶*Simon Fraser University, Vancouver, British Columbia, Canada and York University, Toronto, Ontario, Canada*

⁷*University of Science and Technology of China, Hefei, People's Republic of China*

⁸*Universidad de los Andes, Bogotá, Colombia*

⁹*Charles University, Faculty of Mathematics and Physics, Center for Particle Physics, Prague, Czech Republic*

¹⁰*Czech Technical University in Prague, Prague, Czech Republic*

¹¹*Center for Particle Physics, Institute of Physics, Academy of Sciences of the Czech Republic, Prague, Czech Republic*

¹²*Universidad San Francisco de Quito, Quito, Ecuador*

¹³*LPC, Université Blaise Pascal, CNRS/IN2P3, Clermont, France*

¹⁴*LPSC, Université Joseph Fourier Grenoble 1, CNRS/IN2P3, Institut National Polytechnique de Grenoble, Grenoble, France*

¹⁵*CPPM, Aix-Marseille Université, CNRS/IN2P3, Marseille, France*

¹⁶*LAL, Université Paris-Sud, CNRS/IN2P3, Orsay, France*

¹⁷*LPNHE, Universités Paris VI and VII, CNRS/IN2P3, Paris, France*

¹⁸*CEA, Ifu, SPP, Saclay, France*

¹⁹*IPHC, Université de Strasbourg, CNRS/IN2P3, Strasbourg, France*

²⁰*IPNL, Université Lyon 1, CNRS/IN2P3, Villeurbanne, France and Université de Lyon, Lyon, France*

²¹*III. Physikalisches Institut A, RWTH Aachen University, Aachen, Germany*

²²*Physikalisches Institut, Universität Freiburg, Freiburg, Germany*

²³*II. Physikalisches Institut, Georg-August-Universität Göttingen, Göttingen, Germany*

²⁴*Institut für Physik, Universität Mainz, Mainz, Germany*

²⁵*Ludwig-Maximilians-Universität München, München, Germany*

²⁶*Fachbereich Physik, Bergische Universität Wuppertal, Wuppertal, Germany*

²⁷*Panjab University, Chandigarh, India*

²⁸*Delhi University, Delhi, India*

²⁹*Tata Institute of Fundamental Research, Mumbai, India*

³⁰*University College Dublin, Dublin, Ireland*

³¹*Korea Detector Laboratory, Korea University, Seoul, Korea*

³²*CINVESTAV, Mexico City, Mexico*

³³*FOM-Institute NIKHEF and University of Amsterdam/NIKHEF, Amsterdam, The Netherlands*

³⁴*Radboud University Nijmegen/NIKHEF, Nijmegen, The Netherlands*

³⁵*Joint Institute for Nuclear Research, Dubna, Russia*

³⁶*Institute for Theoretical and Experimental Physics, Moscow, Russia*

³⁷*Moscow State University, Moscow, Russia*

³⁸*Institute for High Energy Physics, Protvino, Russia*

³⁹*Petersburg Nuclear Physics Institute, St. Petersburg, Russia*

⁴⁰*Stockholm University, Stockholm, Sweden and Uppsala University, Uppsala, Sweden*

⁴¹*Lancaster University, Lancaster LA1 4YB, United Kingdom*

⁴²*Imperial College London, London SW7 2AZ, United Kingdom*

⁴³*The University of Manchester, Manchester M13 9PL, United Kingdom*

⁴⁴*University of Arizona, Tucson, Arizona 85721, USA*

⁴⁵*University of California Riverside, Riverside, California 92521, USA*

⁴⁶*Florida State University, Tallahassee, Florida 32306, USA*

⁴⁷*Fermi National Accelerator Laboratory, Batavia, Illinois 60510, USA*

⁴⁸*University of Illinois at Chicago, Chicago, Illinois 60607, USA*

⁴⁹*Northern Illinois University, DeKalb, Illinois 60115, USA*

⁵⁰*Northwestern University, Evanston, Illinois 60208, USA*

- ⁵¹Indiana University, Bloomington, Indiana 47405, USA
⁵²Purdue University Calumet, Hammond, Indiana 46323, USA
⁵³University of Notre Dame, Notre Dame, Indiana 46556, USA
⁵⁴Iowa State University, Ames, Iowa 50011, USA
⁵⁵University of Kansas, Lawrence, Kansas 66045, USA
⁵⁶Kansas State University, Manhattan, Kansas 66506, USA
⁵⁷Louisiana Tech University, Ruston, Louisiana 71272, USA
⁵⁸Boston University, Boston, Massachusetts 02215, USA
⁵⁹Northeastern University, Boston, Massachusetts 02115, USA
⁶⁰University of Michigan, Ann Arbor, Michigan 48109, USA
⁶¹Michigan State University, East Lansing, Michigan 48824, USA
⁶²University of Mississippi, University, Mississippi 38677, USA
⁶³University of Nebraska, Lincoln, Nebraska 68588, USA
⁶⁴Rutgers University, Piscataway, New Jersey 08855, USA
⁶⁵Princeton University, Princeton, New Jersey 08544, USA
⁶⁶State University of New York, Buffalo, New York 14260, USA
⁶⁷Columbia University, New York, New York 10027, USA
⁶⁸University of Rochester, Rochester, New York 14627, USA
⁶⁹State University of New York, Stony Brook, New York 11794, USA
⁷⁰Brookhaven National Laboratory, Upton, New York 11973, USA
⁷¹Langston University, Langston, Oklahoma 73050, USA
⁷²University of Oklahoma, Norman, Oklahoma 73019, USA
⁷³Oklahoma State University, Stillwater, Oklahoma 74078, USA
⁷⁴Brown University, Providence, Rhode Island 02912, USA
⁷⁵University of Texas, Arlington, Texas 76019, USA
⁷⁶Southern Methodist University, Dallas, Texas 75275, USA
⁷⁷Rice University, Houston, Texas 77005, USA
⁷⁸University of Virginia, Charlottesville, Virginia 22901, USA
⁷⁹University of Washington, Seattle, Washington 98195, USA
(Received 3 January 2011; published 25 July 2011)

We present a measurement of the inclusive top quark pair production cross section in $p\bar{p}$ collisions at $\sqrt{s} = 1.96$ TeV utilizing data corresponding to an integrated luminosity of 5.3 fb^{-1} collected with the D0 detector at the Fermilab Tevatron Collider. We consider final states containing one high- p_T isolated electron or muon and at least two jets, and we perform three analyses: one exploiting specific kinematic features of $t\bar{t}$ events, the second using b -jet identification, and the third using both techniques to separate the $t\bar{t}$ signal from the background. In the third case, we determine simultaneously the $t\bar{t}$ cross section and the ratio of the production rates of W + heavy flavor jets and W + light flavor jets, which reduces the impact of the systematic uncertainties related to the background estimation. Assuming a top quark mass of 172.5 GeV, we obtain $\sigma_{t\bar{t}} = 7.78^{+0.77}_{-0.64}$ pb. This result agrees with predictions of the standard model.

DOI: 10.1103/PhysRevD.84.012008

PACS numbers: 14.65.Ha, 12.38.Qk, 13.85.Qk

I. INTRODUCTION

The inclusive $t\bar{t}$ production cross section ($\sigma_{t\bar{t}}$) is predicted in the standard model (SM) with a precision of 6% to 8% [1–5]. Because of the large mass of the top quark, many models of physics beyond the SM predict observable effects in the top quark sector which can affect the top

quark production rate. For example, the decay of a top quark into a charged Higgs boson and a b quark ($t \rightarrow H^+ b$) would affect the value of $\sigma_{t\bar{t}}$ extracted from different final states [6–8]. In the SM, the top quark decays with almost 100% probability into a W boson and a b quark.

In this article, we present a new measurement of the inclusive top quark production cross section in $p\bar{p}$ collisions at $\sqrt{s} = 1.96$ TeV in the lepton + jets (ℓ + jets) final state where one of the W bosons from the top quark decays hadronically into a $q\bar{q}'$ pair and the other leptonically into $e\nu_e$, $\mu\nu_\mu$, or $\tau\nu_\tau$. We consider both direct electron and muon decays, as well as secondary electrons and muons from τ decay, but not taus decaying hadronically. If both W bosons decay leptonically, this leads to a dilepton final state containing a pair of electrons, a pair of muons, or an electron and a muon, all of opposite electric charge. If

*Visitor from Augustana College, Sioux Falls, SD, USA.

†Visitor from The University of Liverpool, Liverpool, UK.

‡Visitor from SLAC, Menlo Park, CA, USA.

§Visitor from ICREA/IFAE, Barcelona, Spain.

||Visitor from Centro de Investigacion en Computacion - IPN, Mexico City, Mexico.

¶Visitor from ECFM, Universidad Autonoma de Sinaloa, Culiacán, Mexico.

**Visitor from Universität Bern, Bern, Switzerland.

only one of the leptons is reconstructed, the dilepton decay chain is also included in the signal. We also include events where both W bosons decay leptonically, and one lepton is an electron or muon and the other a hadronically decaying τ lepton. The $t\bar{t}$ processes where both W bosons decay hadronically contribute to multijet production, which is considered as a background process in this analysis.

We measure the $t\bar{t}$ production cross section using three methods: (i) a “kinematic” method based on $t\bar{t}$ event kinematics, (ii) a “counting” method using b -jet identification, and (iii) a method utilizing both techniques, referred to as the “combined” method. The first method does not rely on the identification of b quarks while the second and third methods do. Thus they are sensitive to different systematic uncertainties. The combined method allows for the simultaneous measurement of the $t\bar{t}$ production cross section and of the composition of the largest background source, $W + \text{jets}$ production.

The analysis is based on data collected with the D0 detector [9] in Run II of the Fermilab Tevatron Collider with an integrated luminosity of $5.3 \pm 0.3 \text{ fb}^{-1}$. The results of this analysis supersede our previous measurement [10], which was done with one-fifth of the data set considered here. A result from the CDF Collaboration in the same $t\bar{t}$ final state with comparable integrated luminosity is available in Ref. [11]. Recently the CDF Collaboration presented a new analysis in which the $t\bar{t}$ production cross section is extracted from a simultaneous fit to a jet flavor discriminant across different samples defined by the number of jets and b tags, constraining many systematic uncertainties [12]. This results in a precision on $\sigma_{t\bar{t}}$ comparable to the measurement presented here. The ATLAS and CMS Collaborations recently reported first measurements of the $t\bar{t}$ cross section in pp collisions at $\sqrt{s} = 7 \text{ TeV}$ [13,14], using data corresponding to integrated luminosities of about 3 pb^{-1} .

In 2006, the D0 detector was substantially upgraded: A new calorimeter trigger was installed [15] and a new inner layer was added to the silicon microstrip tracker [16]. We split the data into two samples: Run IIa before this upgrade (on which our previous $t\bar{t}$ cross section measurement was performed) and Run IIb after it. The corresponding integrated luminosities are 1 and 4.3 fb^{-1} , respectively.

II. D0 DETECTOR

The D0 detector contains a tracking system, a calorimeter, and a muon spectrometer [9]. The tracking system consists of a silicon microstrip tracker (SMT) and a central fiber tracker (CFT), both located inside a 1.9 T superconducting solenoid. The design provides efficient charged-particle tracking in the detector pseudorapidity region $|\eta_{\text{det}}| < 3$ [17]. The SMT provides the capability to reconstruct the $p\bar{p}$ interaction vertex (PV) with a precision of about $40 \mu\text{m}$ in the plane transverse to the beam direction, and to determine the impact parameter of any

track relative to the PV [18] with a precision between 20 and $50 \mu\text{m}$, depending on the number of hits in the SMT, which is key to lifetime-based b -jet tagging. The calorimeter has a central section covering $|\eta_{\text{det}}| < 1.1$, and two end calorimeters (EC) extending the coverage to $|\eta_{\text{det}}| \approx 4.2$. The muon system surrounds the calorimeter and consists of three layers of tracking detectors and scintillators covering $|\eta_{\text{det}}| < 2$ [19]. A 1.8 T toroidal iron magnet is located outside the innermost layer of the muon detector. The luminosity is calculated from the rate of $p\bar{p}$ inelastic collisions measured with plastic scintillator arrays, which are located in front of the EC cryostats.

The D0 trigger is based on a three-level pipeline system. The first level consists of hardware and firmware components. The microprocessor-based second level combines information from the different detector components to construct simple physics objects, whereas the software-based third level uses the full event information obtained with a simplified reconstruction [20].

III. EVENT SELECTION

This analysis uses data from running periods in which all components of the detector (SMT, CFT, calorimeter, and muon system) were fully operational. Events in the $e + \text{jets}$ channel are triggered by requiring either a single electron trigger with a p_T threshold ranging from 15 to 80 GeV, or an electron and a jet with the relaxed electron p_T requirements ranging from 15 to 25 GeV and a jet p_T threshold ranging between 15 and 30 GeV. In the $\mu + \text{jets}$ channel events are triggered by requiring a muon and a jet in Run IIa with a muon p_T threshold between 3 and 8 GeV and a jet p_T threshold between 15 and 30 GeV, and single muon triggers in Run IIb with a muon p_T threshold ranging from 10 to 15 GeV.

Offline, the data samples are enriched in $t\bar{t}$ events by requiring more than one jet of cone radius $\mathcal{R} = 0.5$ [21] reconstructed with the “Run II cone” algorithm [22], with transverse momentum $p_T > 20 \text{ GeV}$ and pseudorapidity $|\eta_{\text{det}}| < 2.5$. Furthermore, we require one isolated electron with $p_T > 20 \text{ GeV}$ and $|\eta_{\text{det}}| < 1.1$, or one isolated muon with $p_T > 20 \text{ GeV}$ and $|\eta_{\text{det}}| < 2.0$ and missing transverse energy $E_T > 20(25) \text{ GeV}$ in the $e + \text{jets}$ ($\mu + \text{jets}$) channel. The higher minimum E_T in the $\mu + \text{jets}$ channel is chosen as it improves the agreement between the data and the background model, in particular, the modeling of the transverse W mass distribution that is sensitive to the multijet background. The PV must be within 60 cm of the detector center in the longitudinal coordinate so that it is within the SMT fiducial region. In addition, the jet with highest p_T must have $p_T > 40 \text{ GeV}$. The high instantaneous luminosity achieved by the Tevatron leads to a significant contribution from additional $p\bar{p}$ collisions within the same bunch crossing as the hard interaction. To reject jets from these additional collisions, we require all jets in Run IIb to contain at least three tracks within

each jet cone that originate from the PV. Events containing two isolated leptons (either e or μ) with $p_T > 15$ GeV are rejected to avoid overlap with the dilepton channel and suppress the $Z + \text{jets}$ background.

The b jets are identified using a neural network formed by combining variables characterizing the properties of secondary vertices and of tracks with large impact parameters relative to the PV [23]. Details of lepton identification, jet identification, and missing transverse energy calculation are described in Ref. [20].

We split the selected $\ell + \text{jets}$ sample into subsamples according to lepton flavor (e or μ) and jet multiplicity, and between Run IIa and Run IIb. For the measurements with b tagging, we split the data into additional subsamples according to the number of tagged b -jet candidates (0, 1, or >1).

IV. SAMPLE COMPOSITION

Top quark pair production and decay is simulated with the ALPGEN Monte Carlo (MC) program [24] assuming a top quark mass of $m_t = 172.5$ GeV (used for all tables and figures in this paper unless stated otherwise). The fragmentation of partons and the hadronization process are simulated using PYTHIA [25]. A matching scheme is applied to avoid double counting of partonic event configurations [26]. The generated events are processed through a GEANT-based [27] simulation of the D0 detector and the same reconstruction programs used for the data. Effects from additional $p\bar{p}$ interactions are simulated by overlaying data from random $p\bar{p}$ crossings over the MC events.

The background can be split into two components: “multijet background,” where the decay products of a final state parton are reconstructed as an isolated lepton, and “electroweak background” that originates from processes with a final state similar to that of the $t\bar{t}$ signal. In the $e + \text{jets}$ channel, background from multijet (MJ) production is when a jet with high electromagnetic content mimics an electron; in the $\mu + \text{jets}$ channel, it occurs when a muon contained within a jet originates from the decay of a heavy-flavor quark (b or c quark), but appears isolated.

The MJ background is estimated from data using the “matrix method” [20]. Two samples of $\ell + \text{jets}$ events are designed categorized by the stringency of the lepton selection criteria: the “tight” (containing N_T events) sample used for the signal extraction is a subset of a “loose” (containing N_L events) set which is dominated by background. The number of MJ events in the tight sample,

$$N_T^{\text{MJ}} = \epsilon_b \frac{\epsilon_s N_L - N_T}{\epsilon_s - \epsilon_b}, \quad (1)$$

is extracted using event counts in these two samples and the corresponding isolated lepton reconstruction and identification efficiencies (ϵ_s) and the probability of misidentifying a jet as a lepton (ϵ_b), determined for Run IIa and Run IIb data separately. The efficiency ϵ_b is measured in a

TABLE I. Efficiencies for isolated leptons and misidentified jets to pass the tight selection criteria. The uncertainties include both statistical and systematic contributions.

	$e + \text{jets}$	$\mu + \text{jets}$
Run IIa		
ϵ_s	0.831 ± 0.011	0.881 ± 0.039
ϵ_b	0.109 ± 0.008	0.172 ± 0.048
Run IIb		
ϵ_s	0.813 ± 0.045	0.896 ± 0.021
ϵ_b	0.124 ± 0.015	0.219 ± 0.043

sample of events that passes the same selection as the signal sample, but has low E_T . This sample is dominated by MJ events, and the remaining contributions from isolated leptons are subtracted. The efficiency ϵ_s is extracted from $W + \text{jets}$ and $t\bar{t}$ MC events calibrated to reproduce lepton reconstruction and identification efficiencies in data. Neither ϵ_b nor ϵ_s shows any statistically significant dependence on the jet multiplicity, and both are obtained from a sample with at least two jets. Table I shows the measured values of ϵ_s and ϵ_b for Run IIa and Run IIb, and Table II provides the numbers of selected loose and tight events in each jet multiplicity bin. The uncertainties on ϵ_s and ϵ_b are dominated by systematic contributions. For ϵ_s we use the maximum difference of the value obtained in the mixed $W + \text{jets}$ and $t\bar{t}$ sample to the value obtained in a pure $W + \text{jets}$ or pure $t\bar{t}$ MC events as uncertainty. For ϵ_b we take into account a potential dependence on E_T , lepton p_T , or the transverse W mass as systematic uncertainty, which results in the dominating contribution to the total uncertainty.

TABLE II. Numbers of selected loose (N_L) and tight (N_T) events used as input for the MJ background estimate as a function of jet multiplicity for samples before and after applying the b -tagging criteria.

	$e + \text{jets}$			$\mu + \text{jets}$		
Run IIa						
	2 jets	3 jets	>3 jets	2 jets	3 jets	>3 jets
N_L	16634	4452	1109	7198	1751	516
N_T	7649	1681	448	5905	1360	390
N_L 1 b tag	996	450	196	413	187	129
N_T 1 b tag	453	198	112	317	140	109
$N_L > 1$ b tag	73	78	45	33	45	38
$N_T > 1$ b tag	48	45	33	28	38	35
Run IIb						
	2 jets	3 jets	>3 jets	2 jets	3 jets	>3 jets
N_L	37472	8153	1914	17581	3457	925
N_T	20423	4118	1012	15290	2904	783
N_L 1 b tag	2917	1130	465	1364	506	278
N_T 1 b tag	1590	648	289	1139	426	236
$N_L > 1$ b tag	251	218	164	125	126	127
$N_T > 1$ b tag	184	154	127	109	114	119

The multivariate technique used in this analysis requires not only the estimate of the MJ background normalization for each jet multiplicity [given by Eq. (1)] but also a model for the kinematic distributions of the MJ background. The latter is obtained from the $\ell + \text{jets}$ data sample of loose leptons that do not fulfill the tight isolation criteria.

The dominant electroweak background is from $W + \text{jets}$ production. Other electroweak backgrounds are single top quark, diboson, and $Z + \text{jets}$ production with $Z \rightarrow \tau\tau$ and $Z \rightarrow ee$ ($Z \rightarrow \mu\mu$) in the $e + \text{jets}$ ($\mu + \text{jets}$) channel. The contributions from these background sources are estimated using MC simulations and normalized to next-to-leading order (NLO) predictions. Diboson events (WW , WZ , and ZZ) are generated with PYTHIA, single top quark production with the COMPHEP generator [28], and $Z + \text{jets}$ events, with $Z \rightarrow ee$, $\mu\mu$, and $\tau\tau$, are simulated using ALPGEN. For the $Z + \text{jets}$ background, the p_T distribution of the Z boson is corrected to match the distribution observed in data, taking into account a dependence on jet multiplicity. All simulated samples are generated using the CTEQ6L1 parton distribution functions (PDFs) [29].

In $W + \text{jets}$ production, the W boson is produced through the electroweak interaction, and additional partons are generated by QCD radiation. Several MC generators are capable of performing matrix element calculations for W boson production including one or more partons in the final state; however these are performed only at tree level. Therefore, the overall normalization suffers from large theoretical uncertainties. For this reason, only the differential distributions are taken from the simulation while the overall normalization of the $W + \text{jets}$ background is obtained from data by subtracting the electroweak and multijet backgrounds and the $t\bar{t}$ signal. This is done as a function of jet multiplicity for each of the analysis channels. The $W + \text{jets}$ contribution is divided into three exclusive categories according to parton flavor: (i) “ $W + \text{hf}$ ” is the sum of all W events with a $b\bar{b}$ or $c\bar{c}$ quark pair and any number of additional jets; (ii) “ $W + c$ ” has events with a W boson produced with a single charm quark and any number of additional jets; and (iii) “ $W + \text{lf}$ ” has W bosons that are produced with light-flavor jets. These three processes are generated by the LO QCD generator ALPGEN. The relative contributions from the three classes of events are determined using NLO QCD calculations based on the MCFM MC generator [30]. We correct the $W + \text{hf}$ ($W + c$) rate obtained from ALPGEN by the calculated K factor of 1.47 ± 0.22 (1.27 ± 0.15) relative to the $W + \text{lf}$ rate. Events from $W + b$ production are included in the $W + \text{lf}$ sample. We do not introduce a separate scale factor for this small contribution.

We validate the NLO QCD calculations for the $W + \text{hf}$ K factor by measuring the experimentally equivalent parameter f_H , defined as a ratio of the observed $W + \text{hf}$ cross section to the ALPGEN LO QCD generator prediction, in control samples which use the same selection criteria as for

the signal sample, but require exactly one or exactly two jets. We extract f_H in the b -tagging analysis by splitting the events into samples without a b -tagged jet and with at least one b -tagged jet. We then adjust f_H iteratively until the prediction matches the data. The resulting f_H value is consistent with the above NLO K factor from MCFM within its statistical uncertainties. In the combined method, on the other hand, we measure f_H simultaneously with the $t\bar{t}$ cross section, assuming the same value of f_H for the $b\bar{b}$ and $c\bar{c}$ components of $W + \text{hf}$. This technique leads to a reduction in uncertainties on the measured value of $\sigma_{t\bar{t}}$.

V. EFFICIENCIES AND YIELDS OF $t\bar{t}$ EVENTS

Selection efficiencies and b -tagging probabilities for each of the $t\bar{t}$ channels are summarized in Tables III and IV, respectively. To calculate these efficiencies, we separate the $\ell + \text{jets}$ $t\bar{t}$ MC events where only one W boson decays to e or μ from the dilepton $t\bar{t}$ events where both W bosons decay leptonically, but only one lepton is reconstructed.

We apply the same b -tagging algorithm to data and to simulated events, but correct the simulation as a function of jet flavor, p_T , and η to achieve the same performance for b tagging as found in the data. These correction factors [23] are determined from data control samples and are used to predict the yield of signal and background events with 0, 1, and >1 b -tagged jets. We also correct lepton and jet

TABLE III. Selection efficiencies for $t\bar{t}$ $\ell + \text{jets}$ and dilepton contributions to the $\ell + \text{jets}$ channels. The selection efficiency is derived using fully simulated MC events corrected to match the performance in data and contains geometric and kinematic acceptance and resolution effects. The uncertainties on the efficiencies from a limited number of MC events are of the order of (1–2)%.

	$e + \text{jets}$			$\mu + \text{jets}$		
	2 jets	3 jets	>3 jets	2 jets	3 jets	>3 jets
$t\bar{t} \rightarrow \ell + \text{jets}$	0.043	0.103	0.097	0.026	0.069	0.070
$t\bar{t} \rightarrow \ell\ell + \text{jets}$	0.108	0.040	0.009	0.067	0.027	0.006

TABLE IV. b -tagging probabilities for $t\bar{t}$ $\ell + \text{jets}$ and dilepton contributions to the $\ell + \text{jets}$ channels corrected to match the performance in data. The uncertainties on the b -tag probabilities from a limited number of MC events are of the order of (1–2)%.

	$e + \text{jets}$			$\mu + \text{jets}$		
	2 jets	3 jets	>3 jets	2 jets	3 jets	>3 jets
$t\bar{t}$ single tagging probabilities						
$t\bar{t} \rightarrow \ell + \text{jets}$	0.431	0.470	0.458	0.417	0.464	0.458
$t\bar{t} \rightarrow \ell\ell + \text{jets}$	0.470	0.459	0.460	0.461	0.456	0.438
$t\bar{t}$ double tagging probabilities						
$t\bar{t} \rightarrow \ell + \text{jets}$	0.068	0.173	0.259	0.066	0.176	0.258
$t\bar{t} \rightarrow \ell\ell + \text{jets}$	0.205	0.241	0.249	0.206	0.246	0.271

identification and reconstruction efficiencies in simulation to match those measured in data.

Table V summarizes the predicted background and the observed numbers of events in $e + \text{jets}$ and $\mu + \text{jets}$ data

with 0, 1, and >1 tags, together with the prediction for the number of $t\bar{t}$ event candidates obtained assuming the production cross section measurement from the combined method.

TABLE V. Yields for $e + \text{jets}$ and $\mu + \text{jets}$ with 0, 1, and >1 b -tagged jets. The number of $t\bar{t}$ events is calculated using the cross section $\sigma_{t\bar{t}} = 7.78$ pb measured by the combined method. Uncertainties include statistical and systematic contributions. Because of the correlations of the systematic uncertainties between the samples, the uncertainty on the total predicted yield is not the sum of the uncertainties of the individual contributions.

Channel	Sample	0 b tags	1 b tag	>1 b tags
$e + 2$ jets	$W + \text{jets}$	$21\,019.1 \pm 517.3$	1369.7 ± 89.8	101.2 ± 13.0
	Multijet	2530.7 ± 301.4	196.7 ± 25.2	5.6 ± 0.7
	$Z + \text{jets}$	1169.5 ± 158.6	68.3 ± 15.3	5.5 ± 2.0
	Other	858.0 ± 84.6	148.4 ± 19.0	21.4 ± 2.6
	$t\bar{t}$	244.8 ± 22.1	265.1 ± 22.6	79.1 ± 8.7
	Total	25821.1 ± 458.2	2038.1 ± 97.4	212.8 ± 18.4
	Observed	25 797	2043	232
$e + 3$ jets	$W + \text{jets}$	3358.1 ± 150.9	315.7 ± 25.7	28.9 ± 3.8
	Multijet	674.9 ± 70.4	75.4 ± 8.4	7.2 ± 0.7
	$Z + \text{jets}$	271.3 ± 39.9	26.1 ± 6.3	2.3 ± 0.9
	Other	171.7 ± 18.4	40.8 ± 5.9	8.6 ± 1.4
	$t\bar{t}$	289.4 ± 27.0	381.4 ± 29.9	147.4 ± 14.2
	Total	4765.3 ± 124.0	839.3 ± 36.8	194.4 ± 15.9
	Observed	4754	846	199
$e + >3$ jets	$W + \text{jets}$	440.0 ± 72.8	54.5 ± 10.0	5.8 ± 1.4
	Multijet	141.0 ± 15.5	22.9 ± 2.9	1.5 ± 0.2
	$Z + \text{jets}$	42.9 ± 7.2	5.6 ± 1.8	0.5 ± 0.2
	Other	30.2 ± 3.9	8.1 ± 1.4	2.1 ± 0.5
	$t\bar{t}$	202.4 ± 24.1	322.0 ± 31.4	180.1 ± 18.5
	Total	856.8 ± 50.9	413.1 ± 25.0	190.1 ± 18.2
	Observed	899	401	160
$\mu + 2$ jets	$W + \text{jets}$	$17\,385.6 \pm 321.0$	1080.8 ± 68.8	80.6 ± 10.3
	Multijet	207.7 ± 117.3	37.5 ± 23.7	1.2 ± 0.8
	$Z + \text{jets}$	1142.0 ± 154.6	68.4 ± 15.4	5.2 ± 1.8
	Other	682.3 ± 67.1	118.5 ± 15.3	17.1 ± 2.3
	$t\bar{t}$	155.3 ± 14.2	162.8 ± 14.0	50.3 ± 6.2
	Total	$19\,572.8 \pm 234.6$	1468.0 ± 77.2	154.3 ± 13.9
	Observed	19 602	1456	137
$\mu + 3$ jets	$W + \text{jets}$	2895.5 ± 100.2	261.1 ± 19.7	23.6 ± 3.0
	Multijet	87.0 ± 28.6	14.1 ± 4.6	0.4 ± 0.2
	$Z + \text{jets}$	221.7 ± 31.3	19.3 ± 4.8	1.8 ± 0.7
	Other	138.0 ± 14.5	32.5 ± 4.5	7.1 ± 1.2
	$t\bar{t}$	197.6 ± 17.5	261.8 ± 21.5	102.8 ± 10.4
	Total	3539.8 ± 77.4	588.8 ± 27.7	135.7 ± 11.7
	Observed	3546	566	152
$\mu + >3$ jets	$W + \text{jets}$	480.8 ± 52.8	62.5 ± 8.2	7.5 ± 1.6
	Multijet	27.3 ± 8.8	5.6 ± 2.1	<0.1
	$Z + \text{jets}$	29.2 ± 5.1	3.8 ± 1.0	1.0 ± 0.5
	Other	22.8 ± 2.8	6.6 ± 1.1	2.1 ± 0.4
	$t\bar{t}$	151.2 ± 16.5	239.9 ± 21.8	134.7 ± 14.4
	Total	711.3 ± 39.5	318.3 ± 17.4	145.3 ± 14.2
	Observed	674	345	154

VI. KINEMATIC METHOD

In this and the following sections we present the methods used to measure the $t\bar{t}$ cross section. The results of the three methods are presented in Sec. X, after a discussion of the sources of systematic uncertainties in Sec. IX.

A. Discrimination

In the kinematic analysis, we use final states with 2, 3, or >3 jets, thereby defining 12 disjoint data sets. To distinguish the $t\bar{t}$ signal from background, we construct a discriminant that exploits differences between kinematic properties of the $t\bar{t} \ell + \text{jets}$ signal and the dominant $W + \text{jets}$ background using the multivariate analysis toolkit TMVA [31]. The multivariate discriminant function is based on a random forest (RF) of decision trees. A decision tree is an extension of a simple cut-based algorithm. It successively applies selection requirements on the input variables, splitting the event sample in two sets (“branches”), which can be split into further categories applying additional requirements, provided there is a sufficient number of events. At the end of this procedure, each event is contained in one of the mutually exclusive categories. At each splitting point, the separation is optimized using a training sample for signal and background. For each event, the output of the decision tree, defined as the ratio of the expected signal over background yield for the final category to which it has been assigned, gives its probability to be a signal event. To reduce the dependence of this tree structure on the composition and the details of the training sample, we use a random forest of decision trees, i.e., a set of decision trees where each one is trained with a random subset of the signal and background training samples. We then apply the “bagging” technique to further improve the stability of the algorithm by repeating the training such that the trained RF represents an average of the outputs of the decision trees. We use 200 trees for the RF, with the boosting type [32] set to bagging, and the separation mode set to the “Gini index” [33]. The separation mode describes the criteria for finding the best separation of signal and background. The Gini index defines the separation by using a product of the purity times one minus the purity in the considered sample.

We split both the $t\bar{t}$ and the $W + \text{jets}$ MC events into two equal samples, and use one for training and testing of the RF discriminant and the other to create discriminant distributions (templates) for fits to data. For all other sources of events, we use the trained RF discriminant to obtain the templates.

We choose input variables that separate signal and background and are well described by the MC simulation. To reduce the sensitivity of variables that are based on the jets in the events to the modeling of soft gluon radiation and to the underlying event, we include only the five highest- p_T

(leading) jets in these definitions. The variables chosen as inputs to build the RF discriminant are as follows:

Aplanarity: The normalized quadratic momentum tensor \mathcal{M} is defined as

$$\mathcal{M}_{ij} = \frac{\sum_o p_i^o p_j^o}{\sum_o |\vec{p}^o|^2},$$

where \vec{p}^o is the momentum vector of a reconstructed object o , and i and j are the three Cartesian coordinates. The sum over objects includes up to the first five jets, ordered by p_T , and the selected charged lepton. The diagonalization of \mathcal{M} yields three eigenvalues $\lambda_1 \geq \lambda_2 \geq \lambda_3$, with $\lambda_1 + \lambda_2 + \lambda_3 = 1$, that characterize the topological distribution of objects in an event. The aplanarity is defined as $\mathcal{A} = \frac{3}{2} \lambda_3$ and reflects the degree of isotropy of an event, with its range restricted to $0 \leq \mathcal{A} \leq 0.5$. Large values correspond to spherically distributed events and small values to more planar events. While $t\bar{t}$ final states are more spherical, as is typical for decays of massive objects, $W + \text{jets}$ and MJ events tend to be more planar.

Sphericity: The sphericity is defined as $\mathcal{S} = \frac{3}{2}(\lambda_2 + \lambda_3)$, and $t\bar{t}$ events tend to have higher values of \mathcal{S} than background events. Values of \mathcal{S} range from zero to one.

H_T^ℓ : The scalar sum of the transverse momenta of up to five leading jets (H_T) and the transverse momentum of the lepton.

H_T^3 : The p_T of the third jet or the scalar sum of the p_T of the jets with the third and fourth, or third to fifth largest p_T in the event, for events with three, four, or more jets, respectively. As these jets correspond largely to gluon radiation for the $W + \text{jets}$ background events but mainly to W decays in the $t\bar{t}$ production, on average H_T^3 has higher values for the latter process.

M_T^{jet} : The transverse mass of the dijet system for $\ell + 2$ jets events. Since H_T^3 is not defined in $\ell + 2$ jets events, we use M_T^{jet} in this channel instead.

M_{event} : The invariant mass of the system consisting of the lepton, the neutrino, and up to five leading jets. The energy of the neutrino is determined by constraining the invariant mass of the lepton and vector E_T (as the neutrino) to the mass of the W boson. Of the two possible solutions for the longitudinal momentum of the neutrino, we use the one with the smaller absolute value. On average, M_{event} is larger for $t\bar{t}$ events than for background.

$M_T^{j_2\nu\ell}$: Transverse mass of the system consisting of the second leading jet, the lepton, and the neutrino, where the energy of the neutrino is determined the same way as in the case of M_{event} .

Figure 1 shows distributions for several of the input variables in the data compared to the sum of expected contributions from $t\bar{t}$ signal and backgrounds for the $\ell + >3$ jets channel. The outputs of the RF discriminant are presented in Fig. 2 for the $\ell + 2$, $\ell + 3$, and $\ell + >3$ jets channels.

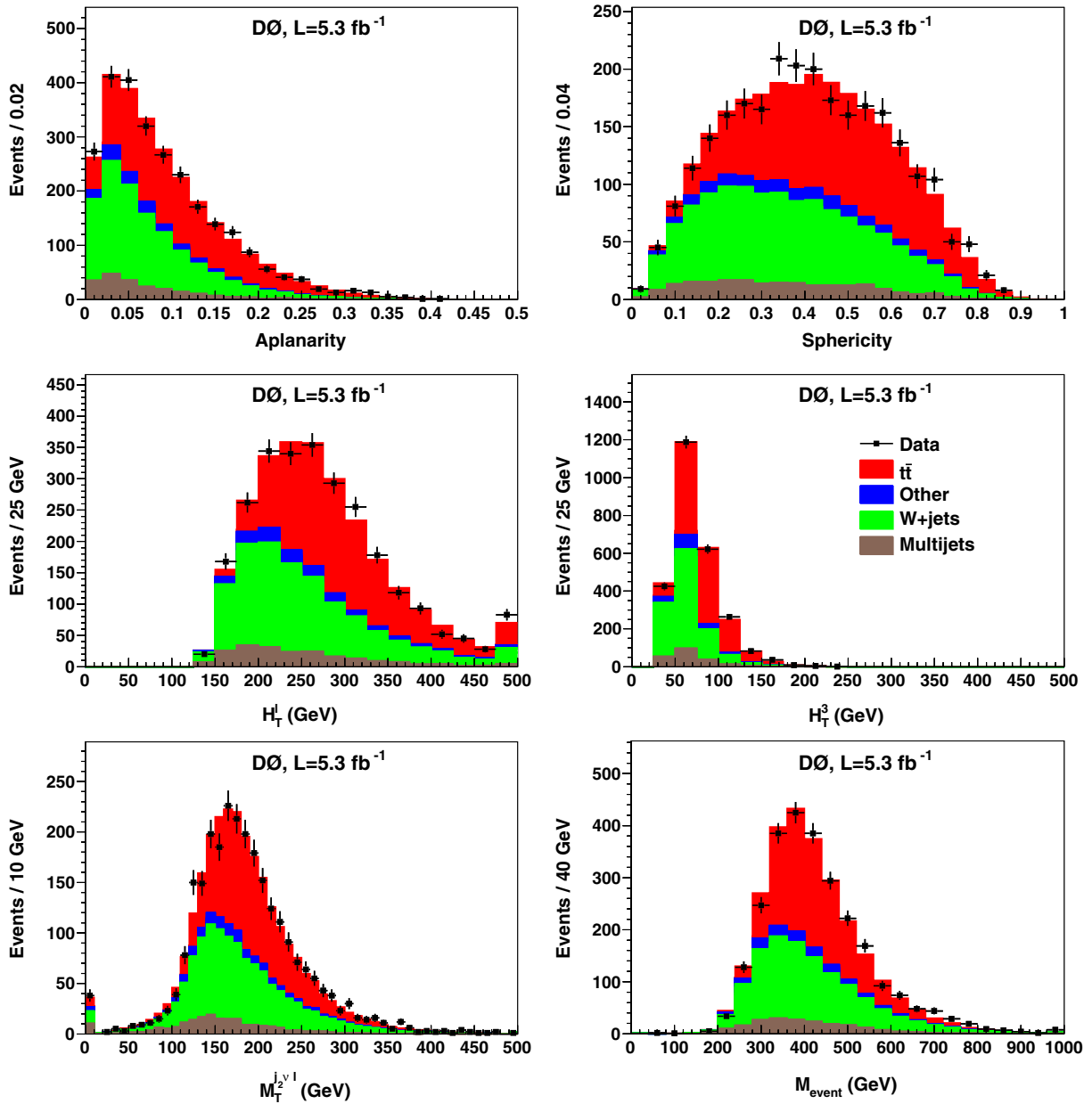


FIG. 1 (color online). Distributions of input variables used in the RF discriminant for the $\ell + >3$ jets channel in data overlaid with the predicted background and $t\bar{t}$ signal calculated using $\sigma_{t\bar{t}} = 7.78$ pb as measured using the combined method. Contributions of the $e + \text{jets}$ and $\mu + \text{jets}$ channels are summed.

Figure 1 indicates good agreement of data with expectation for $m_t = 172.5$ GeV. Similar levels of agreement between data and prediction are observed in all other channels. The normalizations shown in Fig. 2 are based on the results of the kinematic method. The distributions in Figs. 2(a), 2(c), and 2(e) are the results when only fitting $\sigma_{t\bar{t}}$; Figs. 2(b), 2(d), and 2(f) show the result when the $t\bar{t}$ cross section is fitted together with other parameters, as shown in Eq. (2) and described in Sec. VI B.

B. Cross section measurement

To measure the $t\bar{t}$ cross section for the kinematic analysis, we perform a binned maximum likelihood fit of the distributions in the RF discriminant to data. We use templates from MC for dilepton and $\ell + \text{jets}$ contributions to the $t\bar{t}$ signal, as well as for WW , WZ , ZZ , $Z + \text{jets}$, single top quark (s and t channels), and $W + \text{jets}$ backgrounds. The MJ template comes from data, and the amount of MJ background is constrained within the uncertainties resulting from the matrix method.

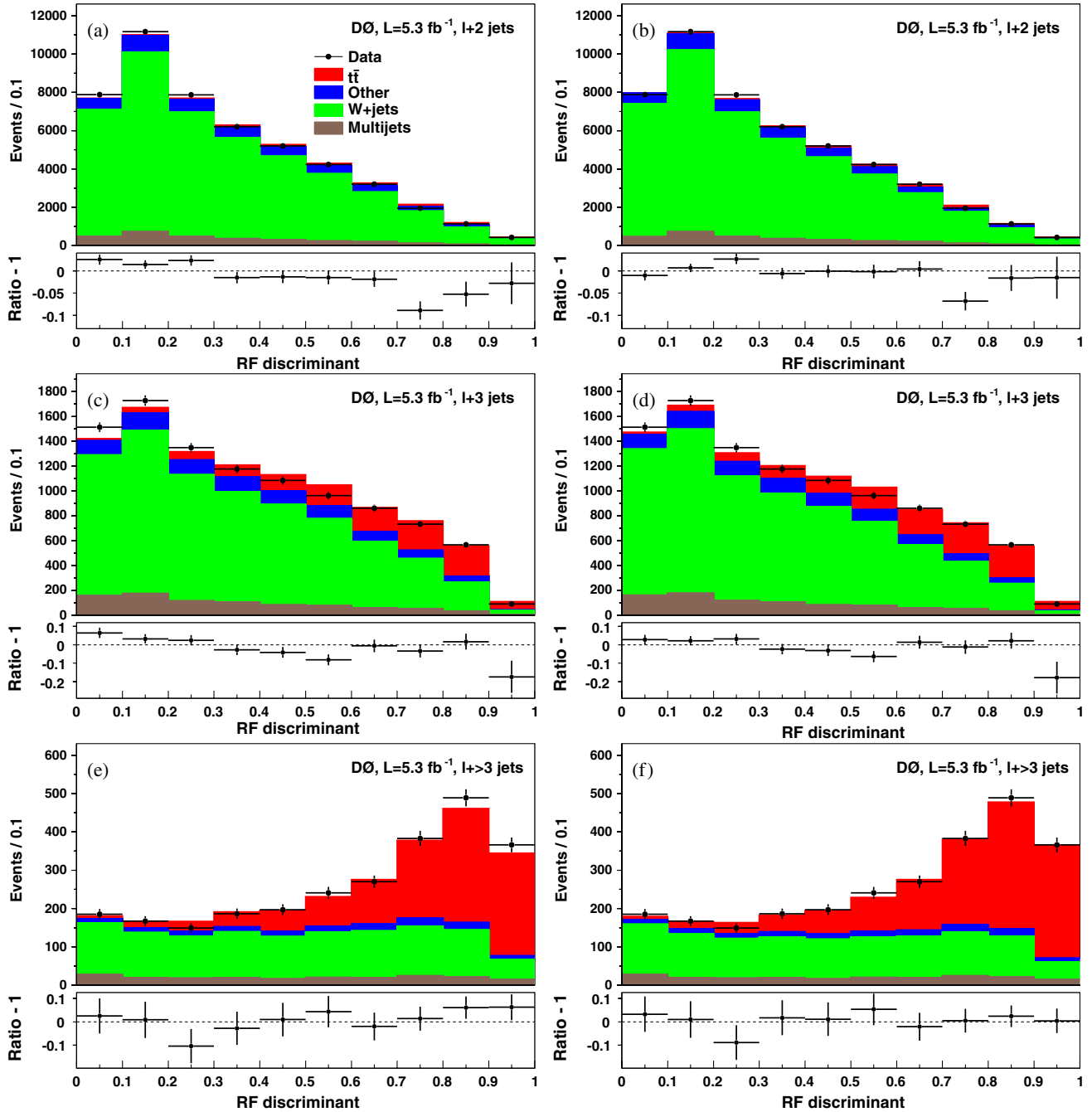


FIG. 2 (color online). Output of the RF discriminant for (a) and (b) $\ell + 2$ jets, (c) and (d) $\ell + 3$ jets, and (e) and (f) $\ell + >3$ jets events, for backgrounds and a $t\bar{t}$ signal based on the cross section obtained with the kinematic method. The ratio of data over MC prediction is also shown. The left plots (a), (c), and (e) show the results with the nuisance parameters fixed at a value of zero. The right plots (b), (d), and (f) show the results when the nuisance parameters are determined simultaneously with the $t\bar{t}$ cross section in the fit. In the left and right plots the contribution from the $t\bar{t}$ signal is normalized to the results of the cross section measurement, $\sigma_{t\bar{t}} = 7.00$ and 7.68 pb, respectively. Contributions of the $e + \text{jets}$ and $\mu + \text{jets}$ channels are summed.

We account for systematic uncertainties in the maximum likelihood fit by assigning a parameter to each independent systematic variation. These “nuisance” parameters are allowed to vary in the maximization of the likelihood function within uncertainties, therefore the measured $t\bar{t}$ cross

section can be different from the value obtained if the parameters for the systematic uncertainties are not included in the fit. The effects of a source of systematic uncertainty that is fully correlated among several channels are controlled by a single parameter in these channels.

The likelihood function is defined as

$$\mathcal{L} = \prod_{j=1}^{12} \left[\prod_i \mathcal{P}^j(n_i^o, \mu_i(\nu_k)) \right] \mathcal{P}^j(N_{\text{LT}}^o, N_{\text{LT}}) \prod_{k=1}^K \mathcal{G}(\nu_k; 0, \text{SD}), \quad (2)$$

where $\mathcal{G}(\nu_k; 0, \text{SD})$ denotes the Gaussian probability density with mean at zero and width corresponding to 1 standard deviation (SD) of the considered systematic uncertainty, $\mathcal{P}(n, \mu)$ denotes the Poisson probability density for observing n events, given an expectation value of μ , N_{LT} denotes the number of events in the loose but not tight (loose–tight) sample. The value of N_{LT} is restricted within Poisson statistics to the observed number of events, N_{LT}^o , in the loose–tight sample, ensuring the inclusion of the statistical uncertainty on the MJ normalization. The first product runs over 12 data sets j and all bins of the discriminant i ; n_i^o is the content of bin i in the selected data sample; and μ_i is the expectation for bin i . This expectation is the sum of the predicted background and the expected number of $t\bar{t}$ events, which depends on $\sigma_{t\bar{t}}$:

$$\mu_i(N_{\text{LT}}^{\bar{t}\bar{t}}, N_{\text{LT}}^W, N_{\text{LT}}^{\text{MC}}, N_{\text{LT}}^{\text{MJ}}) = \mu_i^{\text{ew}}(N_{\text{LT}}^{\bar{t}\bar{t}}, N_{\text{LT}}^W, N_{\text{LT}}^{\text{MC}}) + f_i^{\text{MJ}} N_{\text{LT}}^{\text{MJ}}, \quad (3)$$

with $\mu_i^{\text{ew}}(N_{\text{LT}}^{\bar{t}\bar{t}}, N_{\text{LT}}^W, N_{\text{LT}}^{\text{MC}})$ describing the expected number of events from the electroweak backgrounds and signal:

$$\mu_i^{\text{ew}}(N_{\text{LT}}^{\bar{t}\bar{t}}, N_{\text{LT}}^W, N_{\text{LT}}^{\text{MC}}) = f_i^{\bar{t}\bar{t}} N_{\text{LT}}^{\bar{t}\bar{t}} + f_i^W N_{\text{LT}}^W + \sum_m (f_i^{\text{MC}_m} N_{\text{LT}}^{\text{MC}_m}), \quad (4)$$

and $N_{\text{LT}}^{\bar{t}\bar{t}}$, N_{LT}^W , $N_{\text{LT}}^{\text{MC}}$, and $N_{\text{LT}}^{\text{MJ}}$ being the total number of $t\bar{t}$, W + jets, MC background (diboson, single top quark, Z + jets) and MJ events in the tight lepton sample. Index m in Eq. (4) runs over all backgrounds estimated from MC, and f_i^x is the predicted fraction of contribution x in bin i . The last product of Eq. (2) runs over all independent sources of systematic uncertainties k , with ν_k being the corresponding nuisance parameters and K the total number of independent sources k .

Since the discriminant for the MJ background is not determined from MC simulation but from the loose–tight data sample, it receives a small contribution from events with prompt leptons in the final state:

$$N_{\text{LT}} = N_L - N_T = N_T^s \times \frac{1 - \varepsilon_s}{\varepsilon_s} + N_T^{\text{MJ}} \times \frac{1 - \varepsilon_b}{\varepsilon_b}, \quad (5)$$

where N_T^s is the number of signal-like events in the tight lepton sample, $N_T^s = N_T^{\bar{t}\bar{t}} + N_T^W + N_T^{\text{MC}}$. Then the product $f_i^{\text{MJ}} N_T^{\text{MJ}}$ in Eq. (3) can be calculated as

$$f_i^{\text{MJ}} N_T^{\text{MJ}} = f_i^{\text{LT}} (r \times N_T^s + N_T^{\text{MJ}}) - r \times \mu_i^{\text{ew}}(N_T^{\bar{t}\bar{t}}, N_T^W, N_T^{\text{MC}}), \quad (6)$$

given the fraction of events f_i^{LT} in bin i of the loose–tight data sample and

$$r = \frac{\varepsilon_b}{1 - \varepsilon_b} \frac{1 - \varepsilon_s}{\varepsilon_s}. \quad (7)$$

Thus the contamination of the MJ distribution is taken into account by using the corrected number of events expected in each bin of the discriminant functions used in Eq. (2):

$$\begin{aligned} \mu_i(N_T^{\bar{t}\bar{t}}, N_T^W, N_T^{\text{MC}}, N_T^{\text{MJ}}) \\ = \mu_i^{\text{ew}}(N_T^{\bar{t}\bar{t}}, N_T^W, N_T^{\text{MC}}) + f_i^{\text{LT}} N_T^{\text{MJ}} + r \times [f_i^{\text{LT}} (N_T^{\bar{t}\bar{t}} + N_T^W \\ + N_T^{\text{MC}}) - \mu_i^{\text{ew}}(N_T^{\bar{t}\bar{t}}, N_T^W, N_T^{\text{MC}})]. \end{aligned} \quad (8)$$

We minimize the negative of the log-likelihood function of Eq. (2) as a function of $t\bar{t}$ cross section and the nuisance parameters. The fit results for the $t\bar{t}$ cross section and the nuisance parameters are given by their values at the minimum of the negative log-likelihood function, and their uncertainties are defined from the increase in the negative log-likelihood by one-half of a unit relative to its minimum. Results of the fit are presented in Sec. X.

VII. b -TAGGING METHOD

A. Discrimination

The SM predicts that the top quark decays almost exclusively into a W boson and a b quark ($t \rightarrow Wb$). Hence, besides using just kinematic information, the fraction of $t\bar{t}$ events in the selected sample can be enhanced using b -jet identification. To measure the $t\bar{t}$ cross section, we use final states with exactly three jets and more than three jets and further separate each channel into events with 0, 1, and >1 b -tagged jets, obtaining 24 mutually exclusive data samples.

B. Cross section measurement

As discussed in Sec. IV, before applying b tagging, the contribution from the W + jets background is normalized to the difference between data and the sum of $t\bar{t}$ signal and all other sources of background. Since the W + jets background normalization depends on the $t\bar{t}$ cross section, the measurement of the cross section and the W + jets normalization determination are performed simultaneously. Details of this method, as well as the general treatment of systematic uncertainties, are described in Ref. [34]. The fit of the $t\bar{t}$ cross section to data is performed using a binned maximum likelihood fit for the predicted number of events, which depends on $\sigma_{t\bar{t}}$. The likelihood is defined as a product of Poisson probabilities for all 24 channels j :

$$\mathcal{L} = \prod_{j=1}^{24} \mathcal{P}(n_j, \mu_j) \mathcal{P}^j(N_{\text{LT}}^o, N_{\text{LT}}) \prod_{k=1}^K \mathcal{G}(\nu_k; 0, \text{SD}), \quad (9)$$

and systematic uncertainties are incorporated into the fit in the same way as described in Sec. VI B. Figure 3 shows the distributions of events with 0, 1, and >1 b -tagged jets for events with three and more than three jets in data compared

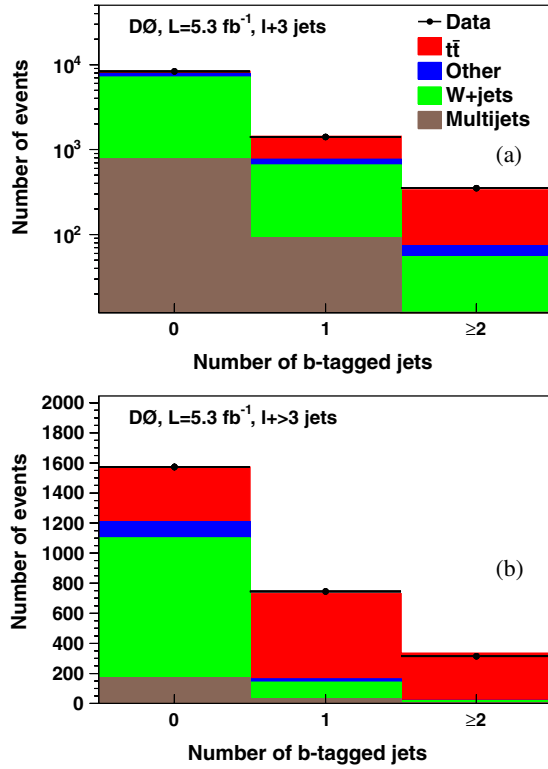


FIG. 3 (color online). Distributions of events with 0, 1, and >1 b -tagged jets for (a) $\ell + 3$ jets and (b) $\ell + >3$ jets, for backgrounds and contributions from $t\bar{t}$ signal for $\sigma_{t\bar{t}} = 8.13$ pb as measured using the b -tagging method. Contributions of the $e +$ jets and $\mu +$ jets channels are summed.

to the sum of predicted background and measured $t\bar{t}$ signal using the b -tagging method. Results for this method are given in Sec. X.

VIII. COMBINED METHOD

In the combined method, kinematic information and b -jet identification are used. We split the selected sample into events with 2, 3, and >3 jets and into 0, 1, and >1 b -tagged jets.

The uncertainty on the background results in a limited contribution of the channels dominated by background to the final $t\bar{t}$ cross section measurement. To improve the sensitivity in such channels, we construct RF discriminant functions as described in Sec. VI, improving the separation of the signal from background. We use the discriminant in all channels with at least three jets, where the background contributes at least half of the total expected number of events.

Events with >2 jets but no b -tagged jet are dominated by the background. For these events we construct a RF discriminant using the same six variables as for the kinematic method described in Sec. VI. For events with three jets and one b tag, we construct discriminants using only \mathcal{A} , H_T^3 , and $M_T^{j_2\nu\ell}$. For all other subchannels, we do not

form RF discriminants, but use the b -tagging method described in Sec. VII. The signal purity is already high in those channels except for the ones with two jets, which do not have a sizable signal contribution and are used to measure the $W +$ jets heavy-flavor scale factor f_H which is the source of one of the largest uncertainties in the b -tagging analysis.

To reduce this source of uncertainty, we measure f_H simultaneously with $\sigma_{t\bar{t}}$, assuming that f_H for $Wb\bar{b}$ production is the same as for $Wc\bar{c}$ production and that it does

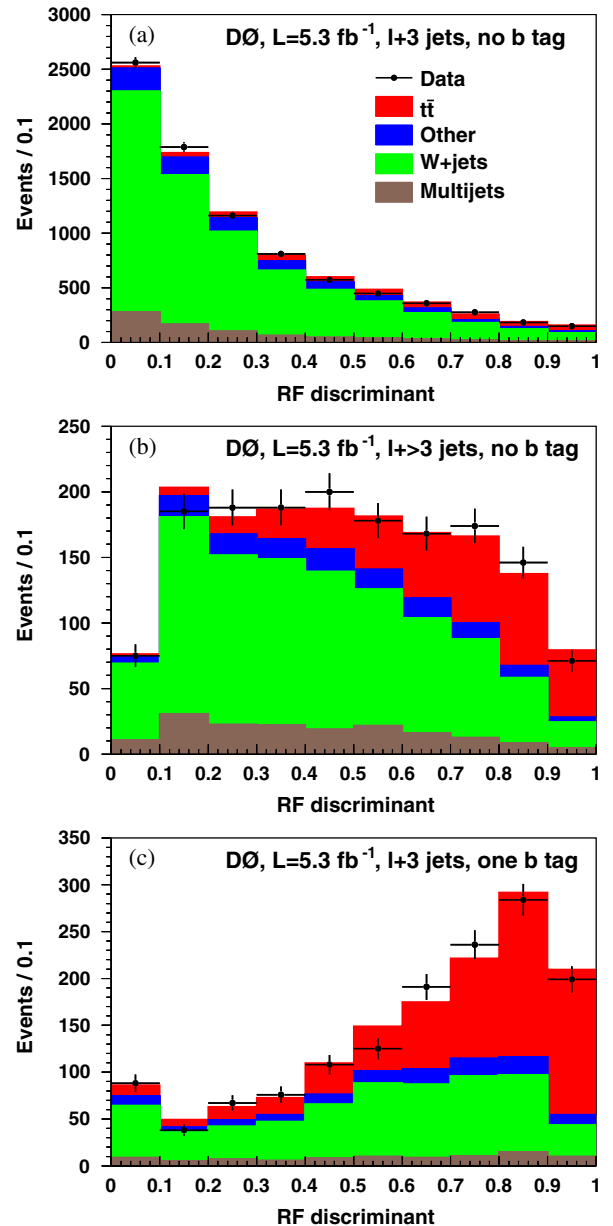


FIG. 4 (color online). Output of the RF discriminant for (a) $\ell + 3$ jets, (b) $\ell + >3$ jets for events without b -tagged jets, and (c) $\ell + 3$ jets with one b -tagged jet, for backgrounds and contributions from the $t\bar{t}$ signal for a cross section of 7.78 pb as measured with the combined method. Contributions of the $e +$ jets and $\mu +$ jets channels are summed.

not depend on the number of jets in the event. Since sources of uncertainty such as light-flavor jet tagging rates are correlated with the value of f_H , and in turn, f_H is anticorrelated with the $t\bar{t}$ cross section, the total uncertainty on the measured $\sigma_{t\bar{t}}$ decreases. The main constraint on f_H is provided by the 2-jets channels with 0, 1, and >1 b -tagged jets. For this reason the RF discriminant was not used for the 2-jets channels in contrast to the measurement using only kinematic information (Sec. VI).

The cross section is measured using the likelihood function of Eq. (2) for channels where a RF discriminant is

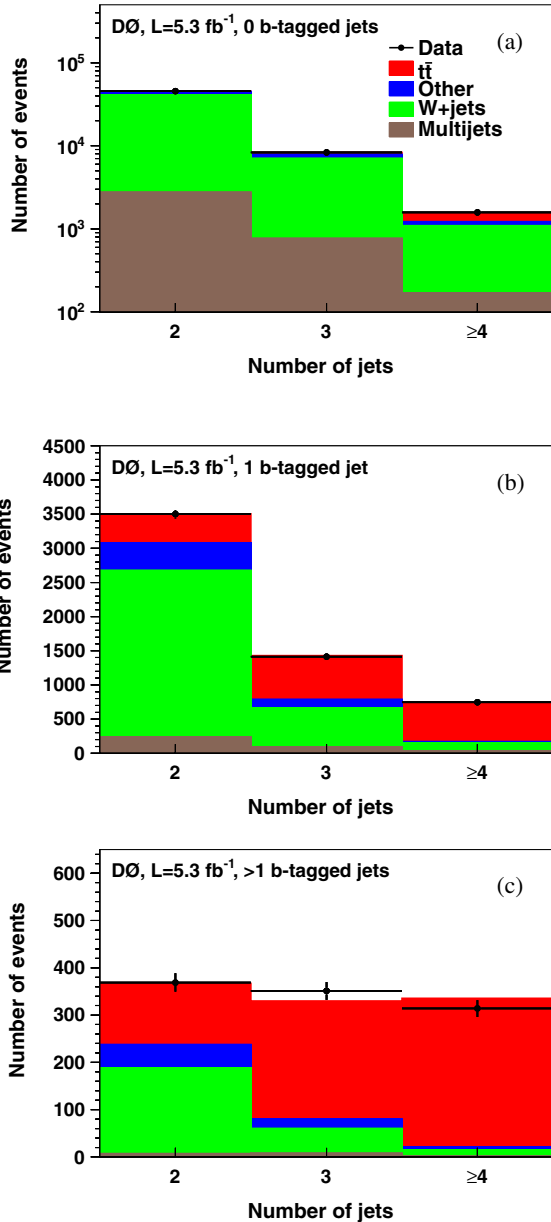


FIG. 5 (color online). Jet multiplicity distributions for events with (a) 0, (b) 1, and (c) >1 b -tagged jets for backgrounds and contributions from the $t\bar{t}$ signal for a cross section of 7.78 pb as measured with the combined method. Contributions of the $e + \text{jets}$ and $\mu + \text{jets}$ channels are summed.

calculated, and using Eq. (9) for all other channels where the b -tagging method is performed. In the minimization procedure, we multiply appropriate likelihood functions for each channel and perform a fit to data assuming the same $t\bar{t}$ cross section for all considered channels. Systematic uncertainties for each channel are incorporated as described in Sec. VIB. The $W + \text{jets}$ heavy-flavor scale factor enters the calculation of the predicted number of $W + \text{jets}$ events, $N(W) \propto N(W + \text{lf}) + f_H N(W + \text{hf}) + f_{Wc} N(W + c)$, where f_{Wc} denotes the NLO K factor for $W + c$ events. A change in f_H results in a change in the predicted number of $W + \text{jets}$ events in each tag category without changing the total number of $W + \text{jets}$ events in the sample prior to applying the b -tagging requirement which is normalized to data.

Figure 4 shows the distribution of the RF discriminant for the $\ell + 3$ jets and $\ell + >3$ jets channels containing no b -tagged jets and for the $\ell + 3$ jets channel containing one b -tagged jet. Figure 5 shows distributions of the number of jets for events with different numbers of b -tagged jets. In both figures we use the measured values of $\sigma_{t\bar{t}}$ and f_H (see Sec. X) as well as the nuisance parameters obtained from the fit.

IX. SYSTEMATIC UNCERTAINTIES

Different sources of systematic uncertainty can affect signal and background normalizations and the shape of the RF discriminant distributions. While some sources of systematic uncertainty affect only one of these categories, several sources of systematic uncertainty can have an effect on both. (All sources of systematic uncertainties considered in the analysis are listed in Tables VII, IX, and XI.) Those sources that affect only signal and background normalizations are as follows: electron and muon identification and trigger efficiencies; MJ background normalization; uncertainties on theoretical cross sections of electroweak backgrounds (listed as “background normalization”); Monte Carlo statistics; the 6.1% luminosity uncertainty [35]; and “other” sources (including modeling of additional $p\bar{p}$ collisions and corrections to the longitudinal distribution of the PV in the MC simulation, as well as data-quality requirements).

Systematic sources affecting both normalization and the shape of the RF discriminant distributions are as follows: signal modeling; b tagging; $V + \text{jets}$ K factor; jet energy scale [36]; jet reconstruction and identification; and MC template statistics.

We take into account all correlations between channels and run periods. All uncertainties are taken as correlated between the channels except for contributions from MC statistics, trigger efficiencies, and the isolated lepton and fake rate required by the matrix method. Systematic uncertainties measured using independent Run IIa and Run IIb data sets and dominated by the limited number of events in these data sets are taken as uncorrelated, including trigger

efficiencies, jet energy scale, jet identification, jet energy resolution, taggability, and lepton identification.

The systematic uncertainties on signal modeling arise from the choice of PDF and the b -fragmentation model, the higher order corrections to the matrix element, and the choice of parton evolution and hadronization models. The uncertainty from the PDF is estimated by evaluating the effect of 20 independent uncertainty PDF sets of CTEQ6.1M [37] on the selection efficiency and b -tagging probabilities, and adding the resulting uncertainties in quadrature. The uncertainty from the b -fragmentation model is evaluated from the difference between tuning of b fragmentation to LEP or SLD data [38]. Signal simulations using ALPGEN or MC@NLO [39] and PYTHIA or HERWIG [40] are used to assess the effect of higher order corrections and parton evolution and hadronization, respectively. The effects from the modeling of color reconnections and initial and final state radiation are evaluated using different PYTHIA tunes and generation parameters. The dominant contribution to the signal modeling originates from the difference between simulations, followed by the PDF uncertainty.

The uncertainties due to b tagging include corrections to the b , c , and light-flavor jet tagging rates, the track multiplicity requirements on jets which are candidates for b tagging (called “taggability”), and on the possible differences in the calorimeter response between b jets and light-flavor jets. A typical fractional per jet uncertainty on the b -jet tagging rate for a jet with p_T between 25 and 80 GeV ranges from 3% to 5%. A similar uncertainty on the light-flavor jet tagging rate is between 8% and 10%.

The uncertainties on the flavor composition of $W +$ jets and $Z +$ jets processes affect the yield and shape of the RF discriminant for these backgrounds. They are determined from variation of the corresponding K factors within their uncertainties and are listed in the “ $V +$ jets K -factor” category.

Jet energy scale, jet energy resolution, and jet reconstruction and identification uncertainties have a large effect on the discriminant distributions for the $W +$ jets background and as a result, a large effect on the measured $\sigma_{t\bar{t}}$. Their influence is reduced by including events with two jets, dominated by the $W +$ jets background, in the fit. Because of the correlation of the considered systematic uncertainties between the different channels, the corresponding nuisance parameters are constrained by the background-dominated 2-jet channels, and affect the result mostly through the samples with more jets, where the $t\bar{t}$ content is higher.

The uncertainties on the MJ background contribution obtained from the matrix method come from systematic uncertainties on ϵ_s and ϵ_b as well as statistical uncertainties due to the limited size of the samples used to model MJ background.

The cross section fit where the contributions of systematic uncertainties are allowed to vary results in a better

agreement between data and the signal plus background prediction for the discriminant distribution in background-dominated samples. An example of this effect is illustrated in Fig. 2, where we perform a comparison of data and the total signal plus background prediction for the case in which only the $t\bar{t}$ cross section is a free parameter of the fit and for the case in which also the nuisance parameters are determined from the fit. Improvements can be seen when the additional parameters associated with systematic contributions are varied.

X. RESULTS

We quote the results for the $t\bar{t}$ cross section measurements using the three different methods described above, assuming a value of the top quark mass of 172.5 GeV. In Sec. XD we discuss the dependence of the cross section measurement on the assumed value of the top quark mass.

A. Kinematic method

Table VI shows the measured cross section in the $e +$ jets and the $\mu +$ jets channels, and for the combined $\ell +$ jets channel for the kinematic method. Table VII lists the corresponding uncertainties. For each category of systematic uncertainties listed in Table VII, only the corresponding nuisance parameters are allowed to vary. The column “Offset” shows the absolute shift of the measured $t\bar{t}$ cross section with respect to the result obtained including only statistical uncertainties. The columns “ $+\sigma$ ” and “ $-\sigma$ ” list the systematic uncertainty on the measured cross section for each category. For the “fit result” all nuisance parameters are allowed to vary at the same time, which can result in a different offset and different uncertainties on the final $t\bar{t}$ cross section than expected from a sum of the individual offsets and systematic uncertainties. The uncertainty given in the row “fit result” refers to the full statistical plus systematic uncertainty.

In the final fit, all nuisance parameters vary by less than one SD from their mean value of zero. This also applies for the two other methods used for the extraction of the cross section.

The consistency of results between the $e +$ jets and $\mu +$ jets channels is studied using an ensemble of 10 000

TABLE VI. Measured $t\bar{t}$ cross section using the kinematic method for separate and combined $\ell +$ jets channels. The first quoted uncertainty denotes the statistical, the second the systematic contribution. The statistical uncertainty is scaled from the statistical only $\sigma_{t\bar{t}}$ result in Table VII to the final $\sigma_{t\bar{t}}$. The total uncertainty corresponds to the one in the row “Fit result” in Table VII.

Channel	$e +$ jets	$\mu +$ jets	$\ell +$ jets
$\sigma_{t\bar{t}}$ (pb)	$6.87 \pm 0.37^{+0.72}_{-0.52}$	$8.04 \pm 0.48^{+0.75}_{-0.59}$	$7.68 \pm 0.31^{+0.64}_{-0.56}$

TABLE VII. Measured $t\bar{t}$ cross section and the breakdown of uncertainties for the kinematic method in the $\ell + \text{jets}$ channel. The offsets show how the mean value of the measured cross section is shifted due to each source of systematic uncertainty. In each line, all but the considered source of systematic uncertainty are ignored. The $\pm\sigma$ give the impact on the measured cross section when the nuisance parameters describing the considered category are changed by ± 1 SD of their fitted value.

Source	$\sigma_{t\bar{t}}$ (pb)	Offset (pb)	$+\sigma$ (pb)	$-\sigma$ (pb)
Statistical only	7.00		+0.28	-0.28
Muon identification		-0.02	+0.05	-0.05
Electron identification		+0.14	+0.13	-0.12
Triggers		-0.08	+0.10	-0.09
Background normalization		+0.07	+0.06	-0.06
Signal modeling		-0.22	+0.20	-0.18
Monte Carlo statistics		+0.00	+0.02	-0.02
MJ background		+0.01	+0.00	-0.05
$V + \text{jets } K$ factor		+0.13	+0.03	-0.03
Jet energy scale		+0.26	+0.00	+0.00
Jet reconstruction and identification		+0.55	+0.18	-0.16
Luminosity		+0.45	+0.50	-0.44
Template statistics		+0.00	+0.04	-0.04
Other		-0.01	+0.13	-0.12
Total systematics			+0.61	-0.55
Fit result	7.68		+0.71	-0.64

generated pseudoexperiments, each representing a single simulation of the results from the data sample, assuming $\sigma_{t\bar{t}}$ measured in the combined $\ell + \text{jets}$ channel. We vary the number of signal and background events in each pseudoexperiment within Poisson statistics about their mean values. For each pseudoexperiment, we measure the cross section in the $e + \text{jets}$ and $\mu + \text{jets}$ channels by performing a likelihood fit in which the parameters corresponding to individual sources of systematic uncertainty are varied randomly according to Gaussian functions, taking into account the correlations between the $e + \text{jets}$ and $\mu + \text{jets}$ channels. We record the difference between $\sigma_{t\bar{t}}$ in both channels and calculate, as a measure of consistency, the probability that it is equal to or larger than the measured difference as shown in Table VI. The two measurements are found to be consistent with a probability of 22%.

B. b -tagging method

Table VIII gives the results of the b -tagging method for the $e + \text{jets}$, $\mu + \text{jets}$, and combined $\ell + \text{jets}$ channels, and Table IX gives the systematic uncertainties. The consistency of these results is checked with pseudoexperiments performed in the same way as described in the previous section. We find that the $\sigma_{t\bar{t}}$ values measured in the $e + \text{jets}$ and $\mu + \text{jets}$ channels are consistent with a probability of 8%.

TABLE VIII. Measured $t\bar{t}$ cross section using b tagging for separate and combined $\ell + \text{jets}$ channels. The first quoted uncertainty denotes the statistical, the second the systematic contribution. The statistical uncertainty is scaled from the statistical only $\sigma_{t\bar{t}}$ result in Table IX to the final $\sigma_{t\bar{t}}$. The total uncertainty corresponds to the one in the row “Fit result” in Table IX.

Channel	$e + \text{jets}$	$\mu + \text{jets}$	$\ell + \text{jets}$
$\sigma_{t\bar{t}}$ (pb)	$7.40 \pm 0.32^{+0.98}_{-0.84}$	$8.78 \pm 0.40^{+1.08}_{-0.92}$	$8.13 \pm 0.25^{+0.99}_{-0.86}$

TABLE IX. Measured $t\bar{t}$ cross section and the breakdown of uncertainties for the b -tagging method in the $\ell + \text{jets}$ channel. The offsets show how the mean value of the measured cross section is shifted due to each source of systematic uncertainty. In each line, all but the considered source of systematic uncertainty are ignored. The $\pm\sigma$ give the impact on the measured cross section when the nuisance parameters describing the considered category are changed by ± 1 SD of their fitted value.

Source	$\sigma_{t\bar{t}}$ (pb)	Offset (pb)	$+\sigma$ (pb)	$-\sigma$ (pb)
Statistical only	7.81		+0.24	-0.24
Muon identification		-0.05	+0.06	-0.05
Electron identification		+0.17	+0.13	-0.13
Triggers		-0.13	+0.11	-0.11
Background normalization		-0.00	+0.08	-0.08
Signal modeling		+0.04	+0.24	-0.27
b tagging		+0.05	+0.34	-0.32
Monte Carlo statistics		-0.01	+0.09	-0.10
MJ background		-0.00	+0.06	-0.06
$V + \text{jets } K$ factor		-0.04	+0.18	-0.19
Jet energy scale		+0.05	+0.09	-0.09
Jet reconstruction and identification		+0.02	+0.17	-0.16
Luminosity		-0.02	+0.53	-0.46
Other		-0.00	+0.14	-0.13
Total systematics			+0.77	-0.72
Fit result	8.13		+1.02	-0.90

C. Combined method

Table X shows results for $\sigma_{t\bar{t}}$ and f_H in $e + \text{jets}$, $\mu + \text{jets}$, and $\ell + \text{jets}$ channels for the combined method and Table XI gives the systematic uncertainties. The relative uncertainties on $\sigma_{t\bar{t}}$ for the combined and the kinematic methods are comparable. This is expected because the measurements are systematically limited. Compared to the kinematic method, the combined method has improved statistical sensitivity. On the other hand, we include more sources of systematic uncertainty, such as the relatively large b -tagging uncertainty, which reduces slightly the final precision.

The fitted value of $f_H = 1.55 \pm 0.09^{+0.17}_{-0.19}$ is in agreement with the theoretical calculation of 1.47 ± 0.22 and with the result obtained by the CDF Collaboration in [12].

TABLE X. Measured $t\bar{t}$ cross section and the $W + \text{jets}$ heavy-flavor scale factor f_H for separate and combined $\ell + \text{jets}$ channels, using both kinematic information and b tagging. The first quoted uncertainty denotes the statistical, the second the systematic contribution. The statistical uncertainty is scaled from the statistical only $\sigma_{t\bar{t}}$ result in Table XI to the final $\sigma_{t\bar{t}}$. The total uncertainty corresponds to the one in the row “Fit result” in Table XI.

Channel	$e + \text{jets}$	$\mu + \text{jets}$	$\ell + \text{jets}$
$\sigma_{t\bar{t}}$ (pb)	$7.22 \pm 0.32^{+0.70}_{-0.63}$	$8.43 \pm 0.39^{+0.80}_{-0.70}$	$7.78 \pm 0.25^{+0.73}_{-0.59}$
f_H	$1.74 \pm 0.13^{+0.21}_{-0.21}$	$1.26 \pm 0.12^{+0.18}_{-0.17}$	$1.55 \pm 0.09^{+0.17}_{-0.19}$

TABLE XI. Measured $t\bar{t}$ cross section and the breakdown of uncertainties for the combined kinematic and b -tagging method in the $\ell + \text{jets}$ channel. The offsets show how the mean value of the measured cross section is shifted due to each source of systematic uncertainty. In each line, all but the considered source of systematic uncertainty are ignored. The $\pm\sigma$ give the impact on the measured cross section when the nuisance parameters describing the considered category are changed by ± 1 SD of their fitted value.

Source	$\sigma_{t\bar{t}}$ (pb)	Offset (pb)	$+\sigma$ (pb)	$-\sigma$ (pb)
Statistical only	7.58		+0.24	-0.24
Muon identification		-0.04	+0.05	-0.05
Electron identification		+0.14	+0.12	-0.12
Triggers		-0.09	+0.09	-0.11
Background normalization		+0.00	+0.07	-0.06
Signal modeling		-0.06	+0.23	-0.21
b tagging		-0.14	+0.12	-0.12
Monte Carlo statistics		-0.01	+0.06	-0.06
MJ background		-0.01	+0.06	-0.04
$V + \text{jets}$ K factor		-0.00	+0.02	-0.02
Jet energy scale		-0.03	+0.00	-0.00
Jet reconstruction and identification		+0.18	+0.18	-0.17
Luminosity		+0.12	+0.51	-0.44
Template statistics		+0.00	+0.03	-0.03
Other		+0.01	+0.14	-0.13
Total systematics			+0.65	-0.58
Fit result	7.78		+0.77	-0.64

D. Top quark mass dependency for the combined method

Different selection efficiencies lead to a dependence of $\sigma_{t\bar{t}}$ on m_t . This is studied using simulated samples of $t\bar{t}$ events generated at different values of m_t using the ALPGEN event generator followed by PYTHIA for the simulation of the parton-shower development. The resulting measurements are summarized in Table XII and can be parametrized as a function of m_t as

TABLE XII. The $t\bar{t}$ cross sections measured using the combined method for different assumed top quark masses. The uncertainty is the combined statistical plus systematic uncertainty.

m_t (GeV)	$\sigma_{t\bar{t}}$ (pb)
150.0	$10.27^{+1.10}_{-0.88}$
160.0	$9.14^{+0.86}_{-0.79}$
165.0	$8.56^{+0.82}_{-0.71}$
170.0	$8.09^{+0.77}_{-0.68}$
172.5	$7.78^{+0.77}_{-0.64}$
175.0	$7.65^{+0.79}_{-0.62}$
180.0	$7.46^{+0.74}_{-0.61}$
185.0	$7.06^{+0.67}_{-0.60}$
190.0	$6.85^{+0.66}_{-0.62}$

$$\sigma_{t\bar{t}}(m_t) = \frac{1}{m_t^4} [a + b(m_t - m_0) + c(m_t - m_0)^2 + d(m_t - m_0)^3], \quad (10)$$

where $\sigma_{t\bar{t}}$ and m_t are in pb and GeV, respectively, and $m_0 = 170$ GeV, $a = 5.78874 \times 10^9$ pb GeV⁴, $b = -4.50763 \times 10^7$ pb GeV³, $c = 1.50344 \times 10^5$ pb GeV², and $d = -1.00182 \times 10^3$ pb GeV.

In Fig. 6 we compare this parametrization to three approximations to $\sigma_{t\bar{t}}$ at next-to-next-to-leading-order (NNLO) QCD that include all next-to-next-to-leading logarithms (NNLL) in NNLO QCD [1,2,4].

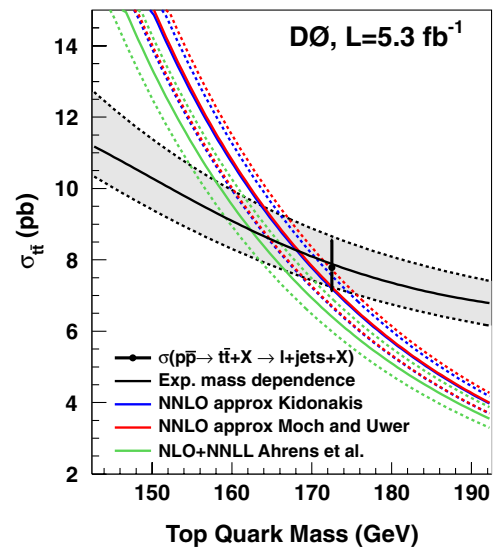


FIG. 6 (color online). Experimental and theoretical [1,2,4] values of $\sigma_{t\bar{t}}$ as a function of m_t . The point shows $\sigma_{t\bar{t}}$ measured using the combined method, the black line shows the fit with Eq. (10), and the gray band with its dashed delimiting lines shows the corresponding total experimental uncertainty. Each curve is bracketed by dashed lines of the corresponding color that represent the theoretical uncertainties due to the choice of PDF and the renormalization and factorization scales (added linearly).

XI. CONCLUSION

We measured the $t\bar{t}$ production cross section in the $\ell + \text{jets}$ final states using different analysis techniques. In 5.3 fb^{-1} of integrated luminosity collected with the D0 detector, for a top quark mass of 172.5 GeV, we obtain

$$\sigma_{t\bar{t}} = 7.78_{-0.64}^{+0.77}(\text{stat} + \text{syst} + \text{lumi}) \text{ pb},$$

using both kinematic event information and b -jet identification and simultaneously measuring the cross section and the ratio of $W + \text{heavy flavor jets}$ to $W + \text{light flavor jets}$. The precision achieved is approximately 9%. A result of similar precision from the CDF Collaboration is available in Ref. [11]. All our results are consistent with the theoretical predictions of $\sigma_{t\bar{t}} = 6.41_{-0.42}^{+0.51} \text{ pb}$ [1] and $\sigma_{t\bar{t}} = 7.46_{-0.67}^{+0.48} \text{ pb}$ [2]. The measured ratio of $W + \text{heavy flavor}$

jets to $W + \text{light flavor jets}$ is consistent with the theoretical NLO calculation and with other measurements [12].

ACKNOWLEDGMENTS

We thank the staffs at Fermilab and collaborating institutions, and acknowledge support from the DOE and NSF (USA); CEA and CNRS/IN2P3 (France); FASI, Rosatom and RFBR (Russia); CNPq, FAPERJ, FAPESP, and FUNDUNESP (Brazil); DAE and DST (India); Colciencias (Colombia); CONACyT (Mexico); KRF and KOSEF (Korea); CONICET and UBACyT (Argentina); FOM (The Netherlands); STFC and the Royal Society (United Kingdom); MSMT and GACR (Czech Republic); CRC Program and NSERC (Canada); BMBF and DFG (Germany); SFI (Ireland); The Swedish Research Council (Sweden); and CAS and CNSF (China).

-
- [1] V. Ahrens, A. Ferroglia, M. Neubert, B.D. Pecjak, and L.L. Yang, *J. High Energy Phys.* **09** (2010) 097; *Nucl. Phys. B, Proc. Suppl.* **205–206**, 48 (2010).
- [2] S. Moch and P. Uwer, *Phys. Rev. D* **78**, 034003 (2008); U. Langenfeld, S. Moch, and P. Uwer, *Phys. Rev. D* **80**, 054009 (2009); M. Aliev *et al.*, *Comput. Phys. Commun.* **182**, 1034 (2011).
- [3] N. Kidonakis and R. Vogt, *Phys. Rev. D* **68**, 114014 (2003).
- [4] N. Kidonakis, *Phys. Rev. D* **82**, 114030 (2010).
- [5] M. Cacciari, S. Frixione, M. L. Mangano, P. Nason, and G. Ridolfi, *J. High Energy Phys.* **04** (2004) 068.
- [6] V.M. Abazov *et al.* (D0 Collaboration), *Phys. Rev. D* **80**, 071102(R) (2009).
- [7] V.M. Abazov *et al.* (D0 Collaboration), *Phys. Lett. B* **682**, 278 (2009).
- [8] A. Abulencia *et al.* (CDF Collaboration), *Phys. Rev. Lett.* **96**, 042003 (2006).
- [9] V.M. Abazov *et al.* (D0 Collaboration), *Nucl. Instrum. Methods Phys. Res., Sect. A* **565**, 463 (2006).
- [10] V.M. Abazov *et al.* (D0 Collaboration), *Phys. Rev. Lett.* **100**, 192004 (2008).
- [11] T. Aaltonen *et al.* (CDF Collaboration), *Phys. Rev. Lett.* **105**, 012001 (2010).
- [12] T. Aaltonen *et al.* (CDF Collaboration), [arXiv:1103.4821](https://arxiv.org/abs/1103.4821) [*Phys. Rev. D* (to be published)].
- [13] G. Aad *et al.* (Atlas Collaboration), *Eur. Phys. J. C* **71**, 1577 (2011).
- [14] V. Khachatryan *et al.* (CMS Collaboration), *Phys. Lett. B* **695**, 424 (2011).
- [15] M. Abolins *et al.*, *Nucl. Instrum. Methods Phys. Res., Sect. A* **584**, 75 (2008).
- [16] R. Angststadt *et al.*, *Nucl. Instrum. Methods Phys. Res., Sect. A* **622**, 298 (2010).
- [17] The rapidity y and pseudorapidity η are defined as functions of the polar angle θ and parameter β as $y(\theta, \beta) \equiv \frac{1}{2} \ln[(1 + \beta \cos\theta)/(1 - \beta \cos\theta)]$ and $\eta(\theta) \equiv y(\theta, 1)$, where β is the ratio of a particle's momentum to its energy. We distinguish detector η (η_{det}) and physics η , where the former is defined with respect to the center of the detector and the latter with respect to the $p\bar{p}$ interaction vertex.
- [18] The impact parameter is defined as the distance of closest approach (d_{ca}) of the track to the PV in the plane transverse to the beam line. The impact parameter significance is defined as $d_{ca}/\sigma_{d_{ca}}$, where $\sigma_{d_{ca}}$ is the uncertainty on d_{ca} .
- [19] V.M. Abazov *et al.*, *Nucl. Instrum. Methods Phys. Res., Sect. A* **552**, 372 (2005).
- [20] V.M. Abazov *et al.* (D0 Collaboration), *Phys. Rev. D* **76**, 092007 (2007).
- [21] \mathcal{R} is defined as $\mathcal{R} = \sqrt{(\Delta\eta)^2 + (\Delta\phi)^2}$.
- [22] G.C. Blazey *et al.*, in *Proceedings of the Workshop: QCD and Weak Boson Physics in Run II*, edited by U. Baur, R.K. Ellis, and D. Zeppenfeld (Fermilab, Batavia, IL, 2000), p. 47, see Sec. 3.5 for details.
- [23] V.M. Abazov *et al.* (D0 Collaboration), *Nucl. Instrum. Methods Phys. Res., Sect. A* **620**, 490 (2010).
- [24] M.L. Mangano, M. Moretti, F. Piccinini, R. Pittau, and A.D. Polosa, *J. High Energy Phys.* **07** (2003) 001.
- [25] T. Sjöstrand, L. Lönnblad, and S. Mrenna, [arXiv:hep-ph/0308153](https://arxiv.org/abs/hep-ph/0308153), we used Version 6.3.
- [26] M.L. Mangano, M. Moretti, F. Piccinini, and M. Treccani, *J. High Energy Phys.* **01** (2007) 013.
- [27] R. Brun and F. Carminati, CERN Program Library Long Writeup W5013, 1993 (unpublished).
- [28] E. Boos *et al.* (CompHEP Collaboration), *Nucl. Instrum. Methods Phys. Res., Sect. A* **534**, 250 (2004).
- [29] J. Pumplin *et al.* (CTEQ Collaboration), *J. High Energy Phys.* **07** (2002) 012.
- [30] J.M. Campbell and R. K. Ellis, *Nucl. Phys. B, Proc. Suppl.* **205–206**, 10 (2010).
- [31] A. Hocker *et al.*, *Proc. Sci., ACAT* (2007) 040 [[arXiv:hep-ph/0703039](https://arxiv.org/abs/hep-ph/0703039)].

- [32] L. Breiman, *Mach. Learn.* **24**, 123 (1996).
- [33] C. Gini, *Variabilità e Mutabilità* (1912), reprinted in *Memorie di Metodologica Statistica*, edited by E. Pizetti and T. Salvemini (Libreria Eredi Virgilio Veschi, Rome, 1955).
- [34] V. M. Abazov *et al.* (D0 Collaboration), *Phys. Rev. D* **74**, 112004 (2006).
- [35] T. Andeen *et al.*, Report No. FERMILAB-TM-2365, 2007.
- [36] V. M. Abazov *et al.* (D0 Collaboration), *Phys. Rev. Lett.* **101**, 062001 (2008).
- [37] D. Stump *et al.*, *J. High Energy Phys.* **10** (2003) 046.
- [38] Y. Peters, K. Hamacher, and D. Wicke, Report No. FERMILAB-TM-2425-E, 2006.
- [39] S. Frixione and B. R. Webber, *J. High Energy Phys.* **06** (2002) 029.
- [40] G. Corcella *et al.*, *J. High Energy Phys.* **01** (2001) 010.